An MR-Safe Endovascular Robotic Platform: Design, Control, and Ex-Vivo Evaluation

Dennis Kundrat, *Member, IEEE*, Giulio Dagnino, Trevor M. Y. Kwok, Mohamed E. M. K. Abdelaziz, Wenqiang Chi, Anh Nguyen, Celia Riga, and Guang-Zhong Yang, *Fellow, IEEE*

Abstract*—Objective: Cardiovascular diseases are the most common cause of global death. Endovascular interventions, in combination with advanced imaging technologies, are promising approaches for minimally invasive diagnosis and therapy. More recently, teleoperated robotic platforms target improved manipulation accuracy, stabilisation of instruments in the vasculature, and reduction of patient recovery times. However, benefits of recent platforms are undermined by a lack of haptics and residual patient exposure to ionising radiation. The purpose of this research was to design, implement, and evaluate a novel endovascular robotic platform, which accommodates emerging non-ionising magnetic resonance imaging (MRI). Methods: We proposed a pneumatically actuated MR-safe teleoperation platform to manipulate endovascular instrumentation remotely and to provide operators with haptic feedback for endovascular tasks. The platform task performance was evaluated in an ex vivo cannulation study with clinical experts ($N = 7$) under fluoroscopic guidance and haptic assistance on abdominal and thoracic phantoms. Results: The study demonstrated that the robotic dexterity involving pneumatic actuation concepts enabled successful remote cannulation of different vascular anatomies with success rates of 90%–100%. Compared to manual cannulation, slightly lower interaction forces between instrumentation and phantoms were measured for specific tasks. The maximum robotic interaction forces did not exceed $3\mathrm{N}$. Conclusion: This research demonstrates a promising versatile robotic technology for remote manipulation of endovascular instrumentation in MR environments. Significance: The results pave the way for clinical translation with device deployment to endovascular interventions using non-ionising real-time 3D MR guidance.

Manuscript received September 11, 2020; revised January 21, 2021 and February 23, 2021; accepted March 5, 2021. Date of publication March 11, 2021; date of current version September 20, 2021. This work was supported by the U.K. EPSRC under Grant EP/N024877/1. *(Dennis Kundrat and Giulio Dagnino contributed equally to this work.) (Corresponding author: Dennis Kundrat.)*

Dennis Kundrat is with the Hamlyn Centre for Robotic Surgery, Imperial College London, SW7 2BU London, U.K. (e-mail: d.kundrat@imperial.ac.uk).

Giulio Dagnino was with the Hamlyn Centre for Robotic Surgery, Imperial College London, U.K. He is now with the University of Twente, The Netherlands.

Trevor M. Y. Kwok and Celia Riga are with the Faculty of Medicine, Department of Surgery and Cancer, Imperial College London, U.K.

Mohamed E. M. K. Abdelaziz, Wenqiang Chi, and Anh Nguyen are with the Hamlyn Centre for Robotic Surgery, Imperial College London, U.K.

Guang-Zhong Yang is with the Institute of Medical Robotics, Shanghai, Jiao Tong University, China.

This article has supplementary downloadable material available at https://doi.org/10.1109/TBME.2021.3065146, provided by the authors.

Digital Object Identifier 10.1109/TBME.2021.3065146

***Index Terms*—Endovascular robotics, MR compatibility, pneumatic actuation, teleoperation, user study.**

I. Introduction

CARDIOVASCULAR diseases (CVD) remain a major health threat in Western countries. According to recent surveys, CVD are the most common cause of death worldwide with 17.9 million deaths each year [1]. CVD include disorders and diseases that affect coronary or peripheral vessels [2]. Without treatment, this condition may cause myocardial infarction or stroke. Nowadays, endovascular interventions are the gold standard of therapy for CVD [3]. Following interdisciplinary clinical and technical research over recent decades, many interventions have become minimally invasive, relying on image guidance for safe navigation through the vasculature. Following attainment of percutaneous vascular access, flexible and thin instruments (guidewires and catheters) are manipulated within the vasculature to access specific branches and targets for diagnosis or therapy, e.g. laser ablation, stent placement, or embolisation [3], [4].

In recent years, extensive clinical interests in robotic assistance have been growing for endovascular procedures [5]. This approach may shorten patient recovery and hospitalisation times owing to less interventional trauma [6]. In comparison to manual instrument manipulation, robotic devices may optimise accuracy, instrument stability, and operator usability. This is further enhanced with motion scaling, elimination of physiological tremor, and most importantly reduction of radiation exposure for clinicians and patients.

Currently available robotic platforms exclusively target conventional fluoroscopy-guided intervention, which has proven feasibility in large patient cohorts but exposes clinicians and patients to ionising radiation [7]. The procedure further applies nephrotoxic contrast agents to selectively outline the vasculature for interventional planning. Those agents may cause nephropathy [8].

In contrast, our research aims at the transition to MR imaging for endovascular guidance due to the following advantages. This not only eliminates the exposure to ionising radiation and use of contrast agents but also provides vascular interventions with both structural and functional soft tissue information, e.g. the vasculature, at a high spatial resolution and contrast [9]. More precisely, MR imaging further complements the procedure with in-situ characterisation of the blood flow, diffusion, temperature variations, perfusion, and oxygenation [10]. In combination with

novel MR instrumentation [11], advantages have been demonstrated for several endovascular applications, such as paediatric deployment [12], [13].

However, the substitution of fluoroscopy in favour of MRI for endovascular interventions is associated with many practical challenges. Firstly, system designs of current MR scanners affect procedural ergonomics as clinical staff cannot directly access and monitor the patient [14]. This provides motivation for additional assistance, e.g. robotics, to manage instrument handling and patient monitoring concurrently. However, assistive devices under consideration must comply with MR safety standards, i.e. elimination of ferromagnetic components [15].

A. Related Work

Thus far, various robotic systems for endovascular or cardiac catheterisation have been proposed in research or commercial applications [5]. These teleoperation platforms commonly consist of master and slave robots. Hence, the device architectures address low levels of robotic autonomy [16].

Commercial platforms usually target application-specific assistance in endovascular and cardiac scenarios. Examples are the *Magellan* and *Sensei* X2 systems (AurisHealth, Redwood city, CA, USA), the *R-one*$^{\text{TM}}$ robot (Robocath, Rouen, France), the Amigo platform (Catheter Precision, Mt. Olive, NJ, USA), and the CorPath GRX platform (Corindus, A Siemens Healthineers Company, Waltham, MA, USA). Operator input to these devices is implemented with human-machine interfaces (HMI). These include multi-DoF joysticks, hand-held devices, or systems with 3D force feedback. Input is further mapped to electromechanical slave kinematics attached to the surgical table. This enables manipulation of customised (steerable) catheters in up to 6 DoF. Clinical trials demonstrated applicability of different platforms [17]–[20]. Beyond that, novel master interfaces were described for optimised teleoperation feedback, transparency, and usability. For example, damping characteristics of magnetorheological fluids were used to mimic and render friction feedback for manual catheter manipulation [21]. Alternatively, manual manipulation of standard catheters was sensed without feedback and was replicated to a remote slave platform [22]. Designs of slave kinematics addressed different electromechanical configurations for instrument manipulation, i.e. translation and rotation, and coupling interfaces [23]–[25]. Platforms for deployment and use in MR environments are still limited and exclusively consider bespoke steerable catheters [26], [27].

B. Contribution

This work focuses on the design and evaluation of a novel endovascular robotic platform with MR safe characteristics. The introduction of MR imaging and its benefits over fluoroscopic imaging to endovascular interventions may pave the way to radiation-free high-resolution diagnosis and treatment. However, as highlighted in Sec. I-A, research in this field is limited. In this regard, we have presented an early-stage robotic prototype in [28] that has been successfully evaluated in an MR environment and demonstrated task feasibility in a preliminary study. Beyond our previous work and based on

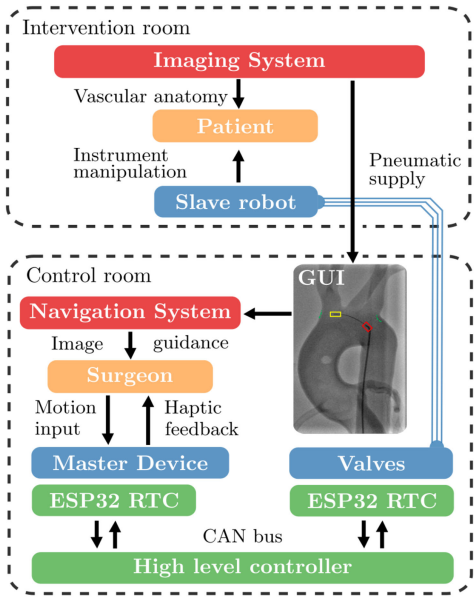

Fig. 1. System architecture of the versatile robotic framework. The surgeon in the control room teleoperates the MR-safe slave robot deployed in the intervention room with the master device. The navigation system provides real-time visual guidance and haptic feedback is rendered through the master device to guide the surgeon during the procedure.

end-user feedback, the next generation of master and slave devices has been equipped with real-time low-level controllers to handle data processing and bus communication. The bus-based device interfacing to a decentralised high-level controller has enabled full system integration and further supports prospective scalability. Additionally, state-of-the-art pneumatic motors have been redesigned and optimised to meet the requirements of frequent clinical use and performance characteristics, e.g. manipulation forces and torques derived from endovascular skill assessment [29]. A user study with clinical experts demonstrates the performance characteristics of the proposed platform and motivates prospective deployment to interventions with MR guidance. The main contributions of this work include: 1) an MR-safe pneumatically-actuated endovascular platform; 2) the integration of a teleoperation and navigation framework; and 3) an ex vivo performance assessment with clinical experts.

The work is structured as follows. Design, control, and navigation of the robotic framework are presented in Sec. II. Further on, the experimental setup and design of the user study are introduced in Sec. III. This is complemented by evaluation methodologies and statistical considerations. Study results in Sec. IV and a discussion in Sec. V underline performance characteristics. Lastly, Sec. VI concludes the work and provides an outlook on future work.

II. Robotic Framework

The general architecture of the robotic framework is summarised in Fig. 1. The robotic platform presents a master-slave configuration and includes the following components: 1) MR-safe slave robot, 2) master device, 3) control workstation, and 4) navigation system. Only the MR-safe slave robot is located in

the interventional room and facilitates instrument manipulation. In contrast, the master device and valve controller are located outside the controlled MR environment to implement remote input and valve-based generation of pneumatic pressure patterns for motor control. Real-time imaging data from fluoroscopy or MR are provided to the operator located in the control room. This enables closed-loop visualisation of operator inputs. Features of master, slave, and control hierarchy are detailed in subsequent sections.

A. Master Device

The main design objective of the master device targets intuitive and remote manipulation of endovascular off-the-shelf instrumentation for optimal teleoperation transparency and procedural assistance. Master kinematics that mimic conventional manual instrument manipulation and feasibility of haptic feedback were targeted, enabling clinicians to control the instruments in a manner already familiar and intuitive to them. This workflow commonly comprises a two DoF motion of catheters and guidewires, i.e. manual linear push/pull displacement and rotation of the extracorporeal section. Inspired by prior master prototypes of our group [28], [30], the proposed device in Fig. 2 has been revised according to expert feedback to match clinical requirements. The core component of the HMI considers a cylindrical handle that substitutes the direct contact between clinician and instrument. Equivalently to physical instrumentation, the handle can be rotated and displaced linearly. The electro-mechanical design applied to both DoF enables the rendering of torque and force feedback. Finite stroke lengths of the linear input are compensated by an automated homing feature. This adapts human motion patterns of concurrent object gripping and manipulation. After linear displacement and sensor-based detection of a terminated action, the handle is homed to the centre of the executable stroke range.

A dual-core ESP32 system-on-the-chip (SoC) controller (Espressif Systems, Shanghai, China) with FreeRTOS operating system implements signal acquisition, signal processing, control, and management of the CAN bus communication. The first core handles signal acquisition, processing, and control tasks. The second core is exclusively dedicated to low latency bus communication.

The user handle contains a torque-resistant linear bushing that is guided on a bespoke slotted shaft (Bosch Rexroth GmbH, Lohr am Main, Germany). This configuration facilitates linear handle displacement x_{M} from operator input. Mechanical characteristics of the bushing concurrently enable angular handle input θ_{M}. This configuration realises operator input in two DoF, i.e. feeding/retraction and angular displacement. This concept enables haptic feedback for both DoF. The latter is generated by linear and rotary brushless DC motors (1247 and 1226 B012, Faulhaber GmbH, Schönaich, Germany). Motor control is provided by motion controllers with CAN interface (MCLM/MCBL 3006, Faulhaber GmbH, Schönaich, Germany). The transmission principle of the slotted shaft motivates stationary drive integration and enhanced manipulation dynamics. The torque feedback rendered to the gripped handle yields with reduction

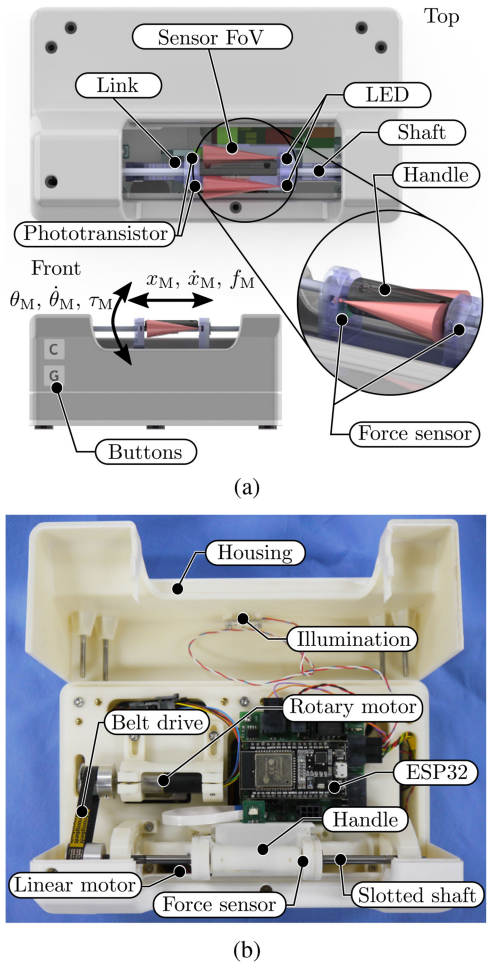

Fig. 2. Master device: (a) Top and front view of CAD model with kinematic annotations and (b) top view of prototype with component exposure. Acronym: Field of view (FoV).

ratios to $\tau_{\mathrm{M}} = i_{\mathrm{G}} i_{\mathrm{P}} \tau_{\mathrm{R}}$, where $i_{\mathrm{G}} = 16$ is the gearhead ratio, $i_{\mathrm{G}} = 1$ is the pulley ratio, and τ_{R} is the motor-sided torque input. Force feedback f_{M} along the handle axis is directly generated under disregard of external disturbances by the linear drive within a maximum stroke of $\pm$ 20 mm.

The interaction between operator and master is detected with two sensor concepts for safety and control. Primarily, operator proximity and contact with the handle are sensed contactless by two opposing pairs of infrared LEDs (VSMY2850 G, Vishay, Malvern, PA, USA) and phototransistors (SFH 3015, Osram AG, Munich, Germany). Each pair forms an optical switch that is mounted to the support structure in parallel to the handle. Operator interaction modulates intensity levels detected by phototransistors. Corresponding voltages are processed by the ESP32 ADC module. A valid grip ρ_{M} is detected if sensor values exceed threshold σ_{G}. Secondly, after device-operator contact is acknowledged, user intentions κ_{M} (feeding, retraction) are extracted from two miniature uniaxial force sensors (FSS1500NSB, Honeywell International Inc., Charlotte, NC, USA) which are located adjacent to both sides of the user handle. The latter are integrated to the support link (see Fig. 2(a)) to measure interaction forces between displaced handle and link.

Sensor voltages are processed with a customised differential amplifier and output voltages are sampled using the ADC of the ESP32 board. A valid operator intention is indicated if sensor values exceed threshold σ_{I}. Based on a preliminary study with novice and expert users, the trigger threshold was determined to 3 N, enabling a robust decoupled manipulation of rotary and linear axis without cross-talk. This is further supported by velocity modulation of the handle from haptic feedback (see Sec. II-D). Two capacitive touch sensors located at the front of the housing enable the operator to switch the driver mode λ_{M} between catheter or guidewire instrumentation. Lastly, the master state yields to

$$\boldsymbol{q}_{\mathrm{M}} = \left(x_{\mathrm{M}}, \theta_{\mathrm{M}}, \dot{x}_{\mathrm{M}}, \dot{\theta}_{\mathrm{M}}, f_{\mathrm{M}}, \tau_{\mathrm{M}}, \rho_{\mathrm{M}}, \kappa_{\mathrm{M}}, \lambda_{\mathrm{M}}\right)^{\mathrm{T}} \in \mathbb{R}^9. \quad (1)$$

Intuitive visual rendering of device states is provided by LED embedded to the housing, e.g. flashing or fading illumination. Generally, ADC acquisition and processing is executed at 200 Hz and 12bit resolution. The module updates the master state in Eq. (1) and error messages on the common CAN bus at 100 Hz and reads CAN data from the high-level controller for settings and diagnostics. It is externally supplied by 24 V. The device footprint is $(191 \times 111 \times 85)\,\mathrm{mm}^3$. Further details are provided in Seq. A of the supplemental video.

B. Design Optimisation of Pneumatic Actuators

MR-safe actuation was implemented in our previous work [28] with linear and rotary pneumatic stepper motors adapted from [31]. These mechanisms contain dual pistons that are acting on a rack or gear. Actuators were fabricated as a whole with additive manufacturing based on the polyjet technology (Objet 500 Connex3, Stratasys Ltd., Eden Prairie, MN, USA) using VeroClear materials in standard quality and glossy surfaces.

Although principles of employed motors enable robust actuation in combination with valve units, the need for design optimisation was identified in our pilot user study [28]. This substantiated to: 1) The use of adhesives for actuator assembly disturbed piston motion and prevented corrective actions. 2) The deficient piston sealing with silicone patches lowered force generation and randomly caused excessive leakage. 3) A reduction of parts desirable to enable advanced fabrication technologies (e.g. injection moulding).

Pressure leaks are mainly due to clearances between additively fabricated pistons and housings to ensure component motion [31], [32]. Sealing was implemented with floating silicone patches in the piston chamber. Although this approach minimises friction, the sealing performance is inferior and may affect generation of piston forces. This also limits multi-actuator networks due to leak accumulation and generates acoustic emissions. The latter lowers the device acceptance in clinical environments. Prior actuators based on rectangular pistons [28], [31] were converted to cylindrical pistons (see Fig. 3(a)). The sealing uses industrial O-rings (1.6/9.3 VITON$^{\mathrm{TM}}$Rubber O-Rings, Simply Bearings, Leigh, U.K.) that are installed to grooves in the piston.

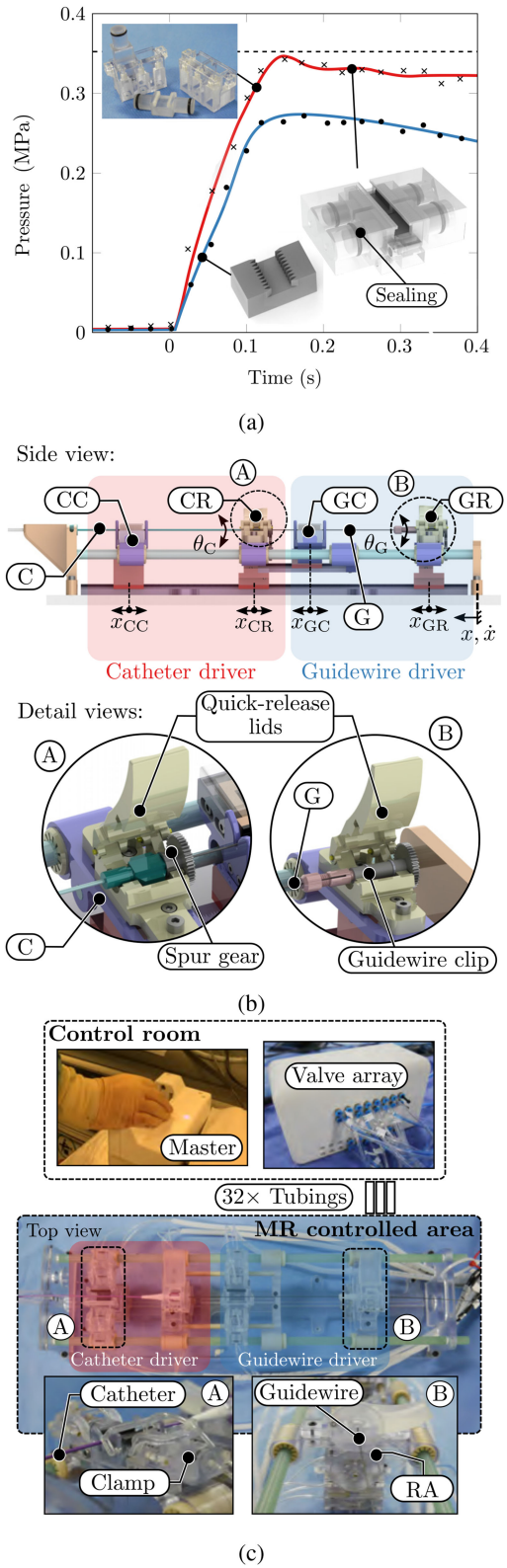

Fig. 3. (a) Pressure-time plots for proposed piston (red), conventional piston (blue), and nominal pressure (dashed). Raw data was fitted with a polynomial. (b) Slave CAD model with kinematic annotations of corresponding platforms and (c) overview and details of a fabricated disposable slave prototype. Acronyms: Catheter (C), guidewire (G), catheter carrier (CC), guidewire carrier (GC), catheter rotation (CR), guidewire rotation (GR), and rotary actuator (RA).

In order to evaluate the design optimisation, pressure responses of actuators (miniaturised T-63) from related work and proposed approach were compared experimentally. Piston chambers of both designs were equipped with pressure gauges (ABPMANN004BGAA5, Honeywell Inc, Charlotte, NJ, USA) and sampled at 1 kHz. A secondary pressure gauge is attached to the reservoir outlet to reference the nominal pressure of 0.35 MPa. Actuators and valves (see Sec. II-C) were connected with tubes of 3 m length in total and composed of a 2 m section with 3 mm outer diameter (PUN-3X0,5-SW, Festo AG, Esslingen, Germany) and 1 m section with 2 mm outer diameter (TU0212C-20, Active Air Automation, Surrey, U.K.).

Following assumptions in [31], both observations have response latencies of 10 ms to 15 ms with a valve contribution of 1.8 ms and tube propagation (length $3\mathrm{m} \approx 9\mathrm{ms}$ latency). Beyond that, the design optimisation demonstrated lower chamber pressure losses from only 10% to 23% with respect to the nominal pressure of 0.35 MPa (see Fig. 3(a)). Beyond pneumatic optimisation, the part number for the linear actuator was reduced by 30%. Reversible actuator assembly was achieved with five PEEK screws (Misumi Europa GmbH, Frankfurt, Germany) after piston mounting. The optimised MR-safe linear actuator is shown in Fig. 3(a). Dimensions are slightly increased to $(47 \times 30 \times 18)\ \mathrm{mm}^3$ to accommodate piston strokes. With a chamber pressure of 0.35 MPa, a piston area $A_\mathrm{P} = 63\mathrm{mm}^2$, and ideal sealing conditions, the piston force results to 18.5 N. The corresponding nominal output force reports to 30.6 N for the linear actuator according to [31] and a wedge ratio of $\alpha = 1.6$. This design was also transferred to rotary actuators and yielded for the given geometry a nominal output torque of 1.15Nm/MPa. The maximal axial force of each clamp without presence of slipping is determined by the estimated friction coefficient (≈ 0.55) of the material pairing between the high-performance rubber inlay (BFG1, Thorlabs Inc., Newton, NJ, USA) of the clamp and the instrument with plastics coating to 10.2 N. Optimisation of pressure responses for rotary mechanisms was achieved at the expense of a slightly increased part number and dimensions. Hence, our robotic platform described in [28] was equipped with optimised pneumatic actuators. A comprehensive accuracy evaluation of this actuator principle is described in [31].

C. MR-Safe Slave Robot

Kinematics of the slave robot mimic manual patterns of instrument handling (catheter/guidewire) in 6 DoF and enable mapping of master input according to Sec. II-D. The device consists of four modular platforms that are attached to a common linear rail as depicted in Fig. 3(b). More specifically, catheter (CC) and guidewire (GC) carriers are dedicated to instrument clamping and linear force transmission for the realisation of insertion and retraction. Both platforms are equipped with pneumatic clamps and linear actuators described in Sec. II-B. Rotary catheter (CR) and guidewire (GR) platforms implement transmission of angular motion to corresponding instruments. Both rotary actuators are further linked to linear actuators that share the common rail. This approach accommodates for instrument displacement and is complemented by the stacked layout of platforms CR and GC. The reader is kindly referred to our preceding work for further design details [28].

Usability and efficient transition from robotic to manual instrument manipulation was facilitated by customised instrument add-ons (see Fig. 3). A bespoke spur gear with Luer lock interface enables direct docking of catheters to platform CR and meshing with the rotary actuator. Similarly, a guidewire clip was implemented for platform GR. Dimensions of add-ons were adapted from off-the-shelf instruments to address versatility. Equivalently to Sec. II-B, structural components were additively fabricated or customised from PEEK material to comply with MR-Safe classification of the American Society for Testing and Materials (ASTM) standard F2503. The footprint of the robot yields $(520 \times 140 \times 120)\ \mathrm{mm}^3$. The robotic prototype was validated in an MR environment as detailed in Sec. SI of the supplemental document.

With respect to the clinical workflow, the design concept of the slave robot targets a cost-effective, intuitive, and fast setup using a single-use robotic technology. After clinical deployment, the slave robot and the associated pneumatic tubing are detached from the valve unit interface in the shielded wall opening of the MR facility. Hence, sterilisation of the platform and tubing becomes obsolete. Due to applied design principles and actuator technology, a direct transition to manufacturing with injection moulding is feasible.

An array of 14 5/2-way directional pneumatic valves (MHA2-MS1H-5/2-2, Festo AG, Esslingen, Germany) handles independent piston motion of employed actuators and clamps (see Fig. 3(c)). Valve switching is triggered by a customised real-time valve controller based on two ESP32 controllers (see Sec. II-A). Both controllers are linked to the common CAN bus and hardware timers on each controller enable independent control of three pneumatic motors with signal sequences described in Sec. II-D. The primary core is dedicated to monitoring and settings adjustment for signal generation. The secondary core handles bus communication at 100 Hz. The actual state of the slave robot is consolidated to

$$\boldsymbol{q}_\mathrm{S} = \left(\boldsymbol{x}_\mathrm{C/G}, \boldsymbol{\theta}_\mathrm{C/G}, \boldsymbol{\gamma}_\mathrm{C/G}\right)^\mathrm{T}, \tag{2}$$

where $\boldsymbol{x}_\mathrm{C/G} = (\boldsymbol{x}_\mathrm{C}, \boldsymbol{x}_\mathrm{G})^\mathrm{T}$ is composed of linear platform displacements $\boldsymbol{x}_\mathrm{C} = (x_\mathrm{CC}, x_\mathrm{CR})^\mathrm{T} \in \mathbb{R}^2$ and $\boldsymbol{x}_\mathrm{G} = (x_\mathrm{GC}, x_\mathrm{GR})^\mathrm{T} \in \mathbb{R}^2$ (see Fig. 3(b)), $\boldsymbol{\theta}_\mathrm{C/G} = (\theta_\mathrm{C}, \theta_\mathrm{G})^\mathrm{T} \in \mathbb{R}^2$ describes the angular instrument configuration, and $\boldsymbol{\gamma}_\mathrm{C/G} = (\gamma_\mathrm{C}, \gamma_\mathrm{G})^\mathrm{T} \in \mathbb{R}^2$ is the clamping condition. Examples of instrument manipulation are provided in Seq. B of the supplemental video.

D. Control and Navigation

The control architecture integrates master and slave devices with a high-level controller (see Fig. 1). The latter accommodates the real-time image guidance framework for rendering of haptic feedback.

The high-level control architecture uses a host-target layout with PC (host) and a dedicated real-time controller (target) for algorithmic prototyping. Host and target are linked via Ethernet interface. The main controller is implemented on a real-time

FPGA target (compactRIO 9022, National Instruments, TX, USA). The target delegates CAN messages between the master device and the slave valve controller. Beyond that, the controller computes the velocity mapping to the slave kinematics from actual master input. General mapping $\mathbb{R}^2 \rightarrow \mathbb{R}^3$ of the two DoF input to the three DoF slave kinematics is given for each instrument by

$$\dot{\boldsymbol{q}}_{\mathrm{S}} = \begin{pmatrix} \dot{\boldsymbol{x}}_{\mathrm{C/G}} \\ \dot{\boldsymbol{\theta}}_{\mathrm{C/G}} \end{pmatrix} = \begin{pmatrix} 1 & 0 \\ 1 & 0 \\ 0 & 1 \end{pmatrix} \begin{pmatrix} S_{\mathrm{t}} & 0 \\ 0 & S_{\mathrm{a}} \end{pmatrix} \begin{pmatrix} \dot{x}_{\mathrm{M}} \\ \dot{\theta}_{\mathrm{M}} \end{pmatrix} \in \mathbb{R}^3, \quad (3)$$

with adaptive linear and angular input scaling $S_{\mathrm{t}} \in \mathbb{R}_{>0}$ and $S_{\mathrm{a}} \in \mathbb{R}_{>0}$. Hence, valve trigger frequencies for linear and angular actuators are computed to $f_{\mathrm{t}} = \dot{x}_{\mathrm{S}}/s_{\mathrm{t}}$ and $f_{\mathrm{a}} = \dot{\theta}_{\mathrm{S}}/s_{\mathrm{a}}$, respectively. Linear and angular step sizes are determined from the actuator design to $s_{\mathrm{t}} = 0.3\mathrm{mm}$ and $s_{\mathrm{a}} = 10°$.

Paired signals are offset with constant phase shift $\phi = 0.25$ at duty cycle $\eta = 0.5$. Valve trigger frequencies are restricted to a maximum of 40 Hz. The multi-channel ($12\times$) trigger output for control of six actuators is generated by customised timer modules on two ESP32 boards. Prior to experimental deployment, all actuators are commanded to a homing procedure using hard stop referencing.

Additionally, an image-based navigation system introduced in [33] was considered for the generation of active constraints rendered through haptic feedback on the master device. In contrast to common teleoperation scenarios with sensing integrated to the slave hardware, this feedback is generated from image metrics and/or user input.

Primarily, the system enables to display the image stream grabbed from the fluoroscope (DVI2USB3, Epiphan Video, Ottawa, Canada) in a customised GUI and to derive parameters for force and torque computation. Instrument tip and vessel walls were tracked in acquired sequences, as described in [33]. The operator observed a viscous friction that increased proportionally with the tip-vessel distance. Thus, a decreasing distance of instrument and vessel causes increased feedback forces and/or torques. The viscous model is given for linear and angular DoF by:

$$\dot{x}_{\mathrm{M}} = \frac{1}{\kappa_{\mathrm{d}}\kappa_{\nu}} I_{\mathrm{M,t}} \quad (4)$$

$$\dot{\theta}_{\mathrm{M}} = \frac{1}{\kappa_{\mathrm{d}}\kappa_{\nu}} I_{\mathrm{M,a}}, \quad (5)$$

where $I_{\mathrm{M,t}}$ and $I_{\mathrm{M,a}}$ are the sensed currents of the linear and rotary motor when the operator applies a force/torque on the master handle. Parameters $\dot{x}_{\mathrm{M}}$ and $\dot{\theta}_{\mathrm{M}}$ are nominal control outputs and product $\kappa_{\mathrm{d}}\kappa_{\nu} > 0$ sets the damping of virtual contacts. The distance of the instrument tip and vessel wall determines κ_{d} and the pose of the tip with respect to the vessel parameter κ_{ν}. Algorithmic details are provided in [28], [33].

III. User Study

The device performance was evaluated in a user study with vascular surgeons and senior vascular surgery registrars. This section outlines the experimental setting and workflow. Secondly, evaluation methodologies and statistical considerations are presented.

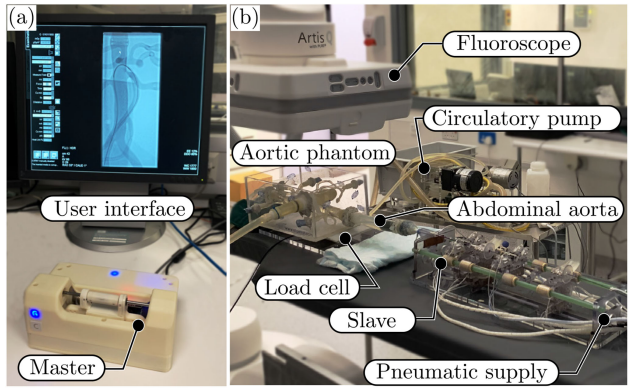

Fig. 4. Experimental setup of user study: (a) Master device with user interface in control room and (b) slave robot deployed to phantom installed in fluoroscopic monitoring.

A. Experimental Setup

The user study was conducted in a research cardiovascular imaging suite using a single-plane fluoroscope (Artis Q ceiling, Siemens Healthineers, Erlangen, Germany). The latter featured a detector panel size of (30×40) cm^2 with a sensor array of (1920×2480) px resulting in 156 μm resolution.

For trials with remote teleoperation, the master device was located in the control room in the proximity of the proprietary user interface of the fluoroscope, as shown in Fig. 4 a. This provided subjects with direct X-ray monitoring of instrument motions in the phantom environment from user inputs to the master device.

Two different anatomical phantoms were considered for simulation of abdominal and thoracic vascular scenarios. The abdominal phantom (A-S-N-003, Elastrat Sàrl, Geneva, Switzerland) is depicted in Fig. 5(a) and comprises the abdominal aorta and iliac arteries with major branch arteries. Percutaneous vascular access was simulated with the placement of an introducer in the femoral artery connector of the model (see Fig. 5(a)). The thoracic aorta and supra-aortic branches were simulated by a thoracic phantom (T-S-N-004, Elastrat Sàrl, Geneva, Switzerland). The abdominal aortic section in this model was substituted by a bespoke aortic section (see Fig. 4 b) that replicates anatomical distances.

Phantoms are located in the head area of the fluoroscope's floating top table. Models are placed on a radiolucent platform rigidly linked to a load cell (Mini40, ATI Industrial Automation, Apex, NC, USA). This facilitated measurements of interaction forces between phantom and vascular instrumentation. Phantoms were mechanically decoupled from the slave robot with a percutaneous introducer sheath that was inserted to corresponding model inlets.

Both phantoms were connected to a circulatory pump (FAIN Biomedical Inc., Nagoyashi, Japan) to simulate physiological pulsatile blood flow and pressure conditions. A surfactant (Elastrat Sàl, Geneva, Switzerland) was added to the water tank

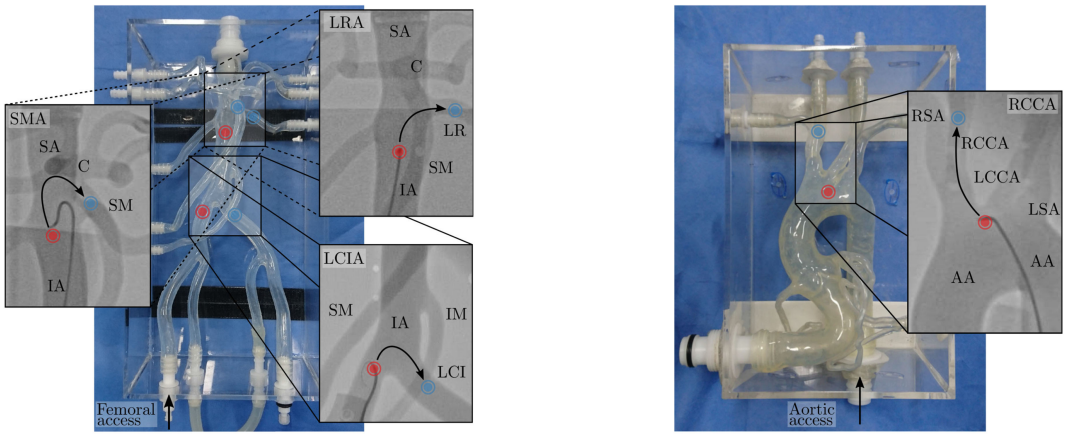

(a) (b)

Fig. 5. Phantom setup and task conditions: (a) Abdominal phantom with LCIA, LRA, and SMA tasks. (b) Thoracic phantom with RCCA task. Red markers denote start configurations and blue markers denote the nominal cannulation targets. Acronyms: infrarenal aorta (IA), suprarenal aorta (SA), superior mesenteric (SM), inferior mesenteric (IM), celiac artery (C), left subclavian artery (LSA), aortic arch (AA), right subclavian artery (RSA), left subclavian artery (LSA), aortic arch (AA), and left common carotid artery (LCCA).

(30 vol% concentration) according to manufacturer guidelines to adjust the model friction. The heart rate was set to 50 bpm and peak systolic pressure to approximately 120mmHg.

The slave robot was placed in the centre of the floating table closely located to the percutaneous introducer. Guidewires and task-specific catheters were installed to the slave device, inserted to the introducer, and advanced to specific starting position in the corresponding phantom prior to each trial (see Fig. 5). Air compressor (PT15, Bambi Air Ltd, Birmingham, U.K.) and valve unit were installed in 2 m distance to the foot section of the floating table, i.e. a low-risk distance of 4 m to the imaging unit taking prospective MRI deployment into consideration.

Kinematics data of master and slave robot, interaction forces, and video streams were acquired from the main controller framework and synchronised based on timestamps. Data was stored at 10 Hz, i.e. governed by the maximum frame rate of the fluoroscopic image stream.

B. Study Design

Subjects were recruited from the Department of Vascular Surgery, St Mary's Hospital, London based on Imperial College London (ICL) recruitment guidelines. All participants ($N = 7$) were either fully qualified vascular surgeons, or senior vascular surgery registrars in the final 1-2 years of training. Subjects received written information, and gave their informed consent for participation and post-experimental data analysis. The study was conducted in accordance with ICL ethics and approved by the ICL research ethics committee (approval 19IC5681). Data was recorded and stored anonymously. Prior to each experimental series, subjects were allowed a 5 min familiarisation period with the robotic teleoperation framework and were provided with an induction to the phantom environment for manual trials.

Afterwards, each subject conducted tasks 1) to 3) on the abdominal and task 4) on the thoracic phantom with randomised order of manual or robotic execution (each $N = 4$). The task workflows are derived from instrument handling in angioplasty and involve manipulation of both the catheter and its supporting guidewire. Further instrument details are provided by Tab. SI in the supplemental document. With respect to a clinical deployment, the task objectives are constituted by the catheter motion due to its subsequent exchange with a balloon catheter over the guidewire. The objectives are further detailed in the following list with visual markers in Fig. 5(a) for abdominal and in Fig. 5(b) for aortic tasks:

1) **Left common iliac artery (LCIA)**: The catheter tip is initially located in the right common iliac artery. The tip must traverse the aortic bifurcation and be advanced at least 3 cm into the LCIA.
2) **Superior mesenteric artery (SMA)**: The catheter tip is located in the suprarenal aorta and must be advanced from the starting position to a point in the proximal superior mesenteric artery.
3) **Left renal artery (LRA)**: From a starting position in the infrarenal aorta (3 cm inferior the target vessel), the catheter must be advanced 2 cm into the left renal artery for task completion.
4) **Right common carotid artery (RCCA)**: The task starts with the catheter tip in the aortic arch in proximity to the left common carotid artery (LCCA) origin. To complete the task, the catheter must traverse the brachiocephalic trunk and reach a point in the RCCA 3 cm from its origin.

Subsequent to study participation, subjects were asked to complete the survey listed in Tab. SII of the supplemental document. The questionnaire is composed of 16 statements linked to a 20 point ordinal scale that maps the range of ± 10 from rejection to agreement. The composition relates to NASA task load index protocols [34] and after scenario questionnaires (ASQ) [35].

C. Evaluation Methodology

Acquired visual data of fluoroscopy sequences was post-processed to determine instrument motions. A semi-automatic

instrument tracking framework was implemented with pyramidal pattern matching (NI Vision, LabVIEW 2018, National Instruments, TX, USA) and applied to visual data.

Instrument tips of catheter and guidewire were separately delineated and masked in the first valid frames by experienced subjects that were not involved in the study to generate tracking template $\boldsymbol{T}_{\mathrm{C/G}}$. Matching of template $\boldsymbol{T}_{\mathrm{C/G}}$ to current fluoroscopic image frame $\boldsymbol{I}_i$ was implemented with normalised cross-correlation, where the video sample series is denoted by $i = \{1, \ldots, N\}$ with N acquired frames in total. The centre of the matching result denoted the current instrument position $\boldsymbol{p}_{\mathrm{C/G}}(t_i) = (u, v)^{\mathrm{T}} \in \mathbb{R}^2$, where u and v denote pixel coordinates in the image frame. The remainder of frames in the sequence was subsequently processed automatically. Challenging tracking conditions, e.g. from occlusions or weak appearance, were indicated by tracking metrics and complemented by manual intervention.

Each X-ray sequence was further calibrated geometrically using a cylindrical object with known physical dimensions located in the plane of relevant anatomy [36]. This facilitates pixel-to-metric conversion of image-based measurements. Each pixel coordinate is converted to corresponding metric representation:

$$\boldsymbol{x}_{\mathrm{C/G},i} = \underbrace{\begin{pmatrix} \varepsilon_u & 0 \\ 0 & \varepsilon_v \end{pmatrix}}_{\boldsymbol{\varepsilon}} \boldsymbol{p}_{\mathrm{C/G},i}, \tag{6}$$

where $\boldsymbol{\varepsilon} \in \mathbb{R}^{2\times 2}$ denotes the conversion matrix obtained from the calibration procedure. The assessment of the instrument tracking accuracy in association with the calibration procedure is described in Sec. SII of the supplemental document.

The following paragraph introduces the study metrics. The *overall distance* of the instrument motion is given by accumulation of Euclidean distances of consecutively tracked tip positions:

$$d_{\mathrm{C/G}} = \sum_{i=1}^{N-1} ||\boldsymbol{x}_{\mathrm{C/G},i+1} - \boldsymbol{x}_{\mathrm{C/G},i}||. \tag{7}$$

The *task completion time* $t_{\mathrm{C/G}}$ is determined from assigned timestamps and describes the duration from commencement to successful termination of the specific task (see criteria in Fig. 5), i.e. the subject has reached the corresponding vascular landmark.

Interaction of instrumentation and vascular anatomy was described by resultant forces obtained from load cell measurements. The latter are transformed to a resultant sample with:

$$f_i = \sqrt{f_{x,i}^2 + f_{y,i}^2 + f_{z,i}^2}, \tag{8}$$

where $f_{x,i}$, $f_{y,i}$, and $f_{z,i}$ are uniaxial measurements of the corresponding load cell axes. Force samples were concatenated to measurement vector $\boldsymbol{f} = (f_1, \ldots, f_N)^{\mathrm{T}}$. Hence, *maximum forces* are given by $\widetilde{f} = \max \boldsymbol{f}$ and trial *mean force* yielded to

$$\bar{f} = \frac{\sum_{i=1}^{N} f_i}{N}. \tag{9}$$

D. Statistical Considerations

Inferential statistics were applied to determine the effects of within-subject factors or experimental settings on recorded task metrics. Task metrics are dependent variables of the analysis. The study regards two independent variables: Two-level factor *mode* describes manual or robotic task execution. Factor *measurement* is a four-level representation corresponding to four repeated measurements per task and subject (see Sec. III-B). Statistics target identification of significant differences within data populations linked to factors. This setting determines the applied methodology to parametric multi-way analysis of variances (ANOVA); more specifically to a two-way ANOVA [37]. However, two fundamental assumptions were assessed for individual data sets: 1) presence of outliers and 2) normal distribution of residuals. If assumption 2) is violated, data transformation, e.g. box cox, is feasible.

IV. Results

This section reports experimental results against the chosen study metrics and the user feedback obtained through questionnaires. Exemplary data is provided in Seq. C of the supplemental video.

A. Study Metrics

Objective assessment of the experimental procedures is reported in Fig. 6 and summarised in Tab. I.

An analysis of this data shows that, considering the defined metrics for performance, manual and robotic cannulation of the selected arteries are overall comparable. Columns *Path Length* report the overall instruments displacement for each cannulation task. Considering the catheter path length d_{C}, it is observed that it is slightly higher in robotic manipulations. More in detail, using the robot, the mean catheter path is $\approx 3\,\mathrm{cm}$ longer when cannulating the LCIA, $\approx 9\,\mathrm{cm}$ longer when cannulating the SMA, $\approx 15\,\mathrm{cm}$ longer when cannulating the LRA, and $\approx 16\,\mathrm{cm}$ longer when cannulating the RCCA. On the other hand, results show an average decrease in the guidewire path when using the robot. In detail: $\approx 3\,\mathrm{cm}$ shorter when cannulating the LCIA, $\approx 1\,\mathrm{cm}$ shorter when cannulating the SMA, $\approx 8\,\mathrm{cm}$ longer when cannulating the LRA, and $\approx 1\,\mathrm{cm}$ shorter when cannulating the RCCA. However, results showed that the guidewire path length is never significantly affected by the experimental condition, i.e. manual or robotic deployment. The analysis of catheter path length did show significant differences, excluding the LCIA cannulation. The completion time resulted on average slightly more than $1\,\mathrm{min}$ longer when using the robot, namely: $65\mathrm{s}$ when for cannulating the LCIA, $71\mathrm{s}$ for the SMA, $73\mathrm{s}$ for the LRA, and $95\mathrm{s}$ for the RCCA. These results are statistically significant according to the ANOVA test.

The analysis of manipulation forces (i.e. the forces applied to the phantoms during cannulation tasks) resulted lower when using the robot with respect to manual. Examples of force measurements along the instrument paths for robotic LCIA and RCCA cannulation are provided in Figs. 7(a) and 7(b) and a manual RCCA cannulation in Fig. 7(c). The corresponding

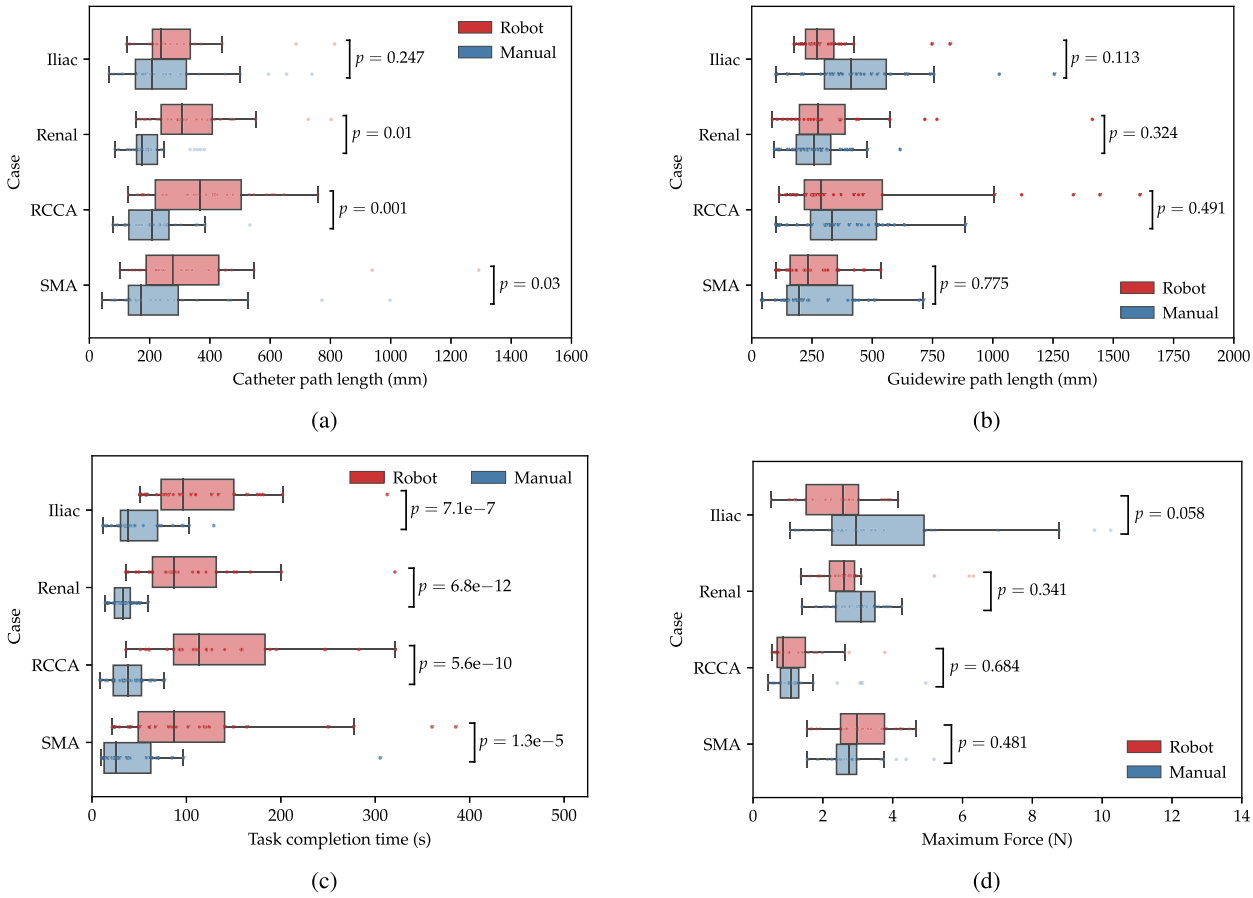

Fig. 6. Boxplots: (a) Catheter path lengths, (b) guidewire path lengths, (c) task completion times, and (d) maximum forces.

TABLE I
USER STUDY METRICS FOR CANNULATION TASKS (MEAN ± SD)

Task	Condition	Path length d_C (mm)	Path length d_G (mm)	Completion time t_C (s)	Mean force $\bar{f}$ (N)	Max force $\tilde{f}$ (N)	Cannulation rate β (%)
LCIA	Manual	264.9 ± 177.9	450.2 ± 267.9	**49.3 ± 29.9*****	0.8 ± 0.7	**3.7 ± 2.5***	100
	Robot	293.8 ± 162.4	313.2 ± 157.4	**115.1 ± 61.4*****	0.5 ± 0.2	**2.5 ± 1.1***	90
SMA	Manual	**258.3 ± 221.0***	268.4 ± 181.2	**44.8 ± 57.5*****	1.0 ± 0.3	2.8 ± 0.8	97
	Robot	**350.0 ± 261.3***	261.8 ± 123.8	**116.4 ± 99.1*****	0.8 ± 0.3	3.0 ± 0.9	90
LRA	Manual	**202.5 ± 82.7****	271.9 ± 120.6	**32.4 ± 11.8*****	0.7 ± 0.2	3.0 ± 0.8	100
	Robot	**348.2 ± 155.8****	355.2 ± 269.4	**105.1 ± 59.0*****	0.7 ± 0.3	2.8 ± 1.2	100
RCCA	Manual	**220.5 ± 109.6*****	370.7 ± 188.6	**39.2 ± 20.1*****	0.4 ± 0.2	1.3 ± 1.0	100
	Robot	**381.8 ± 173.5*****	360.2 ± 303.1	**134.1 ± 73.6*****	0.4 ± 0.2	1.2 ± 0.8	97

Significance levels: $^{*}p \leq 0.05$; $^{**}p \leq 0.01$; $^{***}p \leq 0.001$;

robotic displacement is shown in Figs. S3a and S3b in the supplemental document.

In general, mean forces resulted in 60% lower when cannulating the LCIA, and 25% lower when cannulating the SMA. Mean forces resulted in the same during LRA and RCCA cannulation tasks. However, these results are not statistically significant according to the ANOVA test. Maximum forces resulted significantly lower values when cannulating the LCIA with the robot, showing a decrease of 45% with respect to manual. Similarly, maximum forces are lower in robotic cannulation of LRA and RCCA (7% and 8% respectively) although the ANOVA test did not show statistical significance. Manual cannulation of the SMA resulted in slightly lower maximum forces (7%), but again, not statistically significant. Finally, the cannulation success rate using the robot was 90% in LCIA and SMA cannulation, 100% in LRA cannulation, and 97% in RCCA. The cannulation rate during manual tasks was slightly higher, presenting 100% in LCIA, LRA, and RCCA, and 97% in SMA cannulations. An example of trial-based results is presented in Sec. SIII of the supplemental document.

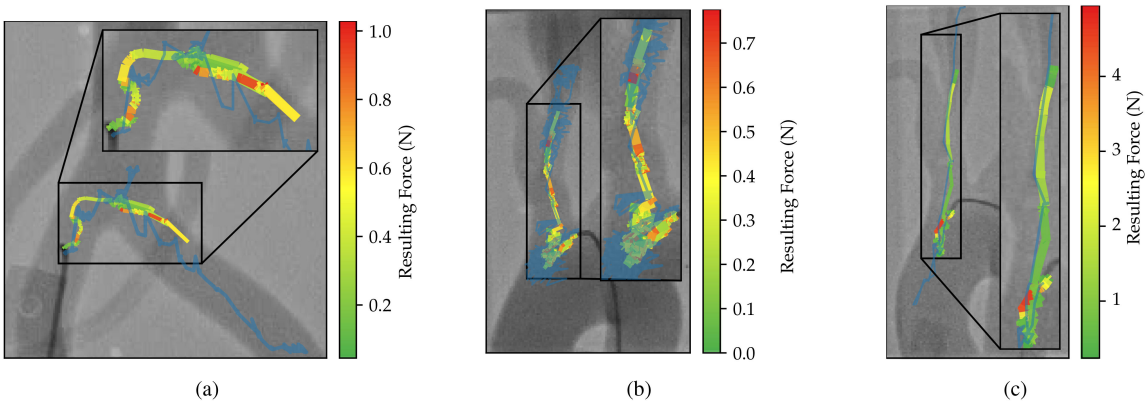

Fig. 7. Force examples: (a) robotic LCIA cannulation, (b) robotic RCCA cannulation, (c) manual RCCA cannulation. Colour overlays correlate tracked catheter tip positions and corresponding force measurements. This enables identification of difficult anatomy or catheter handling issues. Animated study data is provided in Seq. C of the supplemental video.

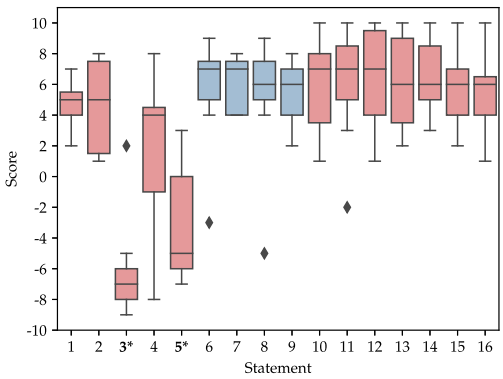

Fig. 8. Survey results. Red plots annotate statements related to design and usability. Blue plots denote task specific statements. Marker * indicates negative statements.

With respect to the protocol of the study series, occasional instrument buckling was present between the introducer and slave robot during the user experiments which resulted from interaction of the instruments and the silicone phantom, i.e. high friction forces from interaction of instruments and model vessels prevented further instrument feeding by the robot.

B. Questionnaire

Results (mean $\pm$ SD) of the post-experimental survey are summarised for all expert users ($N = 7$) in Fig. 8 and are discussed in the following. In general, subjects were satisfied with the system control (S4, 3.8 ± 2.5), the precision (S1, 4.7 ± 1.6), and acknowledged the presence of haptic feedback (S2, 4.6 ± 3.0). Beyond that, the task-specific survey outcomes underline quantitative results. Subjects appreciated their performance in LCIA (S6, 5.4 ± 3.7), LRA (S7, 6.0 ± 1.8), SMA (S8, 5.0 ± 4.3), and RCCA (S9, 5.4 ± 2.0) cannulation tasks. Furthermore, subjects have valued the system introduction (S13, 6.1 ± 3.0), the steep learning phase (S12, 6.4 ± 3.2), low stress (S3, -7.2 ± 1.3), and the straightforward procedural workflow (S11, 6.0 ± 3.9). This also addressed ergonomics (S10, 5.9 ± 3.0) and procedural safety (S5, -4.8 ± 4.2, S14, 6.6 ± 2.4). Future work has been motivated by positive statements on frequent use of the system (S15, 5.7 ± 2.5) and recommendation to peers (S16, 5.4 ± 2.7).

V. Discussion

Experimental results demonstrate the potential of the robotic platform for endovascular interventions. Vision and robotics are seamlessly integrated into the clinical workflow to support the clinician in performing the surgical procedure. Medical images (e.g. fluoroscopy) are used to generate visual and haptic feedback for operator guidance. The intuitiveness and ergonomics of the master manipulator allow the operators to fully leverage their endovascular skills with the dexterity and stability provided by the robotic slave. The metrics chosen for the performance evaluation give an account of the usability and safety of the system. Results on these metrics are reported for both robotic and conventional manual manipulation. However, any direct metric comparison of manual vs robotic procedures must take into account that the trials were conducted by trained surgeons with relevant experience in manual catheterisation but no training with the robotic platform. Results of manual cannulations are a reference for completeness of the work. As reported in Sec. IV-A, surgeons achieved robotic cannulation success rates of 90% - 100%. In the case of unsuccessful trials, two main issues were identified: 1) buckling of the catheter, and 2) finite instrument manipulation strokes. These are both related to design limitations of the slave prototype. Friction between the catheter, the introducer, and the vascular phantom occasionally resulted in buckling of the catheter from insufficient mechanical support. As a result, the surgeon's motion commands on the master robot, although properly replicated by the slave, did not translate to corresponding movement of the catheter tip within the vasculature. The current design of the slave robot further presents a finite linear manipulation stroke that was derived from anatomy. This limits the range of instrument motion. In a few cases, the buckling in Sec. IV, combined with the limited stroke of the slave robot, resulted in an 'out-of-workspace' condition which prevented the surgeon from completing the cannulation. This issue can be fixed with a expandable catheter support located between the slave robot and the percutaneous introducer, e.g. as

in patent US8961533B2. The analysis of mean and maximum forces shows that overall there is a reduction of forces exerted to the phantoms when the robot is used. Forces are very relevant clinically, in terms of patient safety: high-force contact between an instrument and the vessel wall may result in injury or embolisation, which may cause bleeding or loss of blood supply to the vital organs. The forces acquired with our system are overall in line with similar experiments involving experts [29], further corroborating the potential clinical applicability of our platform. From a technical point of view, lower forces can be related to the higher manipulation stability and optimised user input for delicate manoeuvres provided by the robot, and specifically to the vision-based haptic guidance, whose role is actually guiding the surgeon through the vasculature while avoiding high-impact contacts between the endovascular instruments and the vessel walls. Unsurprisingly, completion time is higher when the robot is used with respect to manual cannulations. This is due to two factors: 1) the intrinsically lower dynamics of the robotic system, due to the vision-based architecture which slows down the velocity of the robot when the manipulated instruments approach the vessel wall; and 2) the lack of surgical training with our robotic system. However, with an average completion time of less than 2 min, the results on this metric are already within an acceptable range for actual clinical use.

The robotic platform allows the manipulation of both catheter and guidewire but not simultaneously as in the standard manual procedure. Although this was not perceived as a limitation by the users, it may have forced them to find alternative strategies to accomplish the task. The analysis of travelled instrument distances and experimental videos shows that, when performing cannulation tasks with the robot, the surgeons manipulated the catheter more than the guidewire, whereas in manual cannulations, catheter and guidewire manipulation were more equal. This may be explained by the technical limitations of the robot described above, causing surgeons to adapt their behaviour to work around the limitations, as well as experience considerations, as participants were accustomed to manual procedures but were new to using the robot. A learning effect related to the number of trials may be demonstrated by the RCCA example in Sec. SIII. However, further analysis must include experts and trials to identify significant learning effects. This also addresses effects related to haptic feedback. The latter does not exactly replicate the haptics of manual endovascular procedures as this would include accumulation of tissue-instrument contacts along the instrument bodies and/or introducers. However, the experts acknowledged the transparency of this assistive concept and the study results corroborate its feasibility. Further training with the systems may enable the users to complete the tasks more efficiently.

Despite the comprehensive fluoroscopic image analysis and its promising results, single-plane fluoroscopy not only exposes patient and operator to ionising radiation but further shows limitations with respect to procedural monitoring, e.g. ambiguous representation of instruments or branches of the vasculature, or recovery of instrument poses for accurate pose control in semi-automated procedures. Those ambiguities may be resolved inherently by MRI.

Qualitative user feedback (see Fig. 8) corroborates the results obtained through objective metrics. The survey responses show that the robotic system was well received both in terms of technical design and clinical usability. Further to the data reported in Sec. IV-B and summarised in Fig. 8, subjects individually appreciated the concept of mimicking manual instrument handling and augmentation of 'transparent' but effective haptic feedback. In contrast, automation of procedural sub-tasks, e.g. larger displacements in non-tortuous vessels, was suggested by users to enhance temporal efficiency. Drawbacks resulting from potential pneumatics latencies have not been remarked by the experts.

Overall, this user study demonstrated the feasibility of the proposed robotic system in clinically relevant endovascular tasks. Results provided valuable data for future improvements, highlighting the potential of the robotic platform in clinical translation, but also current limitations. The main technical limitations are related to the catheter buckling and the limited linear operational workspace of the slave robot. While catheter buckling can be easily avoided by adding a guiding slide to the front of the robot, the optimisation of the operational workspace will require a robotic redesign. This will need to take into account the specific intended procedures (as the stroke needed to accomplish cannulation must be factored in) but also the usability. While an enlarged robot would allow a larger stroke, the integration within the clinical workflow would be negatively impacted. The new design will need to be a compromise between these two factors. Although the robotic hardware has demonstrated adequate manipulation performances and already enabled MR deployment, the clinical workflows must adapt to MR environments. This, in particular, addresses the integration of the platform to real time MRI suites. Challenges are mainly dedicated to novel image/volume processing algorithms for haptic guidance and advanced user visualisation. Control schemes of the master may include feed forward approaches to compensate for the internal friction. Beyond that, MR-safe endovascular instrumentation is required.

While the study metrics were designed to obtain quantitative and qualitative analysis of the system performance and usability, they are not a substitute for the actual clinical outcome. There are inherent limitations associated with the use of silicon phantoms, as their biomechanics differ from real tissues, in particular their response to damage. Future studies should use in vivo models, such as porcine models, to provide more data more closely applicable to a real clinical setting. It would be valuable to assess the endothelial injuries caused by the instrument manipulation (e.g. through histopathology [38]), and ideally correlate it to the exerted forces. Future investigations would also benefit from a larger number of users and tasks to strengthen the statistical significance. In terms of system usability, it would be useful to assess the users learning path on the robotic system, including endovascular experts with different levels of robotic experience.

VI. Conclusion

Endovascular interventions are among the most relevant and widely used therapies for cardiovascular diseases. Various

robotic technologies were commercialised to assist the interventional workflow. However, common deficiencies of state-of-the-art technologies are proprietary instrumentation, non-intuitive master consoles, and, importantly, the X-ray exposure for clinicians and patients. This contribution addresses these challenges, demonstrating that expert vascular surgeons were able to successfully complete all cannulation tasks using the proposed platform.

Looking into the future, MRI may replace common X-ray imaging and may be incorporated to the procedural workflow to improve diagnosis, 3D navigation, and eliminate radiation exposure in endovascular applications. Hence, this contribution presents an alternative robotic strategy. We realised a novel highly-integrated robotic concept which consists of a master unit and an MR-safe slave unit. While this study focuses on the comprehensive performance evaluation with clinical experts in a phantom study, the feasibility of safe MR deployment was already demonstrated in our prior work [28]. Our future work addresses: 1) Automation of procedural sub-tasks, e.g. retraction or branch cannulation, for augmentation and enhancement of operator skills as presented in our prior work [39]. 2) Device integration to state-of-the-art MRI suites and fusion with 2D/3D navigation. 3) Incorporation of tailored and dexterous MR-safe steerable catheters and wires, and 4) user studies in MR environments. This may pave the way for successful symbiosis of endovascular robotics and MRI.

References

[1] G. A. Roth *et al.*, "Global, regional, and national age-sex-specific mortality for 282 causes of death in 195 countries and territories, 1980-2017: A systematic analysis for the global burden of disease study 2017," *Lancet*, vol. 392, no. 10159, pp. 1736–1788, Nov. 2018.

[2] J. Kaplan, *Kaplan's Cardiac Anesthesia*, 7th ed. New York, NY, USA: Elsevier, 2017.

[3] W. Moore, *Endovascular Surgery*. New York, NY, USA: Elsevier Saunders, 2011.

[4] P. Schneider, *Endovascular Skills: Guidewire and Catheter Skills for Endovascular Surgery*, 4th ed. Taylor & Francis Group, 2019.

[5] H. Rafii-Tari, C. J. Payne, and G.-Z. Yang, "Current and emerging robot-assisted endovascular catheterization technologies: A review," *Ann. Biomed. Eng.*, vol. 42, no. 4, pp. 697–715, Apr. 2014.

[6] J. Bonatti *et al.*, "Robotic technology in cardiovascular medicine," *Nature Rev. Cardiol.*, vol. 11, no. 5, pp. 266–275, May 2014.

[7] P. Ho *et al.*, "Ionizing radiation absorption of vascular surgeons during endovascular procedures." *J. Vasc. Surg.*, vol. 463, pp. 455–459, 2007.

[8] S. P. Powell *et al.*, "Race, contrast-induced nephropathy and long-term outcomes after coronary and peripheral angiography and intervention," *Cardiovasc. Revascularization Med.*, vol. 19, no. 6, pp. 31–35, 2018.

[9] T. Heidt *et al.*, "Real-time magnetic resonance imaging-guided coronary intervention in a porcine model," *Sci. Rep.*, vol. 9, no. 1, Jun. 2019, Art. no. 8663.

[10] M. Bock and F. K. Wacker, "MR-guided intravascular interventions: Techniques and applications," *J. Magn. Reson. Imag.*, vol. 27, no. 2, pp. 326–338, 2008.

[11] H. C. Clogenson *et al.*, "Multi-selective catheter for MR-guided endovascular interventions," *Med. Eng. Phys.*, vol. 37, no. 7, pp. 623–630, 2015.

[12] A. N. Raval and R. J. Lederman, "Real-time magnetic resonance imaging to guide pediatric endovascular procedures," *Pediatr. Cardiol.*, vol. 26, no. 3, pp. 251–259, Jun 2005.

[13] O. M. Navarro, "Magnetic resonance imaging of pediatric soft-tissue vascular anomalies," *Pediatr. Radiol.*, vol. 46, no. 6, pp. 891–901, May 2016.

[14] F. Fernández-Gutiérrez *et al.*, "Comparative ergonomic workflow and user experience analysis of MRI versus fluoroscopy-guided vascular interventions: An iliac angioplasty exemplar case study," *Int. J. Comput. Assist. Radiol. Surg.*, vol. 10, no. 10, pp. 1639–1650, Oct. 2015.

[15] J. G. Delfino and T. O. Woods, "New developments in standards for MRI safety testing of medical devices," *Curr. Radiol. Rep.*, vol. 4, no. 6, Mar. 2016.

[16] G.-Z. Yang *et al.*, "Medical robotics—Regulatory, ethical, and legal considerations for increasing levels of autonomy," *Sci. Robot.*, vol. 2, no. 4, 2017.

[17] W. Saliba *et al.*, "Novel robotic catheter remote control system: Feasibility and safety of transseptal puncture and endocardial catheter navigation," *J. Cardiovasc. Electrophysiol.*, vol. 17, no. 10, pp. 1102–1105, 2006.

[18] E. M. Khan *et al.*, "First experience with a novel robotic remote catheter system: Amigo mapping trial," *J. Interventional Cardiac Electrophysiol.*, vol. 37, no. 2, pp. 121–129, Aug. 2013.

[19] J. Bismuth *et al.*, "A first-in-man study of the role of flexible robotics in overcoming navigation challenges in the iliofemoral arteries," *J. Vasc. Surg.*, vol. 57, no. 2, pp. 14S–19S, Feb. 2013.

[20] J. F. Granada *et al.*, "First-in-human evaluation of a novel robotic-assisted coronary angioplasty system," *JACC: Cardiovasc. Interv.*, vol. 4, no. 4, pp. 460 – 465, 2011.

[21] S. Guo *et al.*, "A novel robot-assisted endovascular catheterization system with haptic force feedback," *IEEE Trans. Robot.*, vol. 35, no. 3, pp. 685–696, 2019.

[22] Y. Thakur, J. S. Bax, D. W. Holdsworth, and M. Drangova, "Design and performance evaluation of a remote catheter navigation system," *IEEE Trans. Biomed. Eng.*, vol. 56, no. 7, pp. 1901–1908, Jul. 2009.

[23] G. Bian *et al.*, "An enhanced dual-finger robotic hand for catheter manipulating in vascular intervention: A preliminary study," in *Proc. IEEE Int. Conf. Inf. Automat.*, 2013, pp. 356–361.

[24] S. Guo, M. Qin, N. Xiao, Y. Wang, W. Peng, and X. Bao, "High precise haptic device for the robotic catheter navigation system," in *Proc. IEEE Int. Conf. Mechatronics Automat.*, 2016, pp. 2524–2529.

[25] K. Wang *et al.*, "Design and performance evaluation of real-time endovascular interventional surgical robotic system with high accuracy," *Int. J. Med. Robot. Comput. Assist. Surg.*, vol. 14, no. 5, 2018, Paper e 1915.

[26] M. A. Tavallaei *et al.*, "Magnetic resonance imaging compatible remote catheter navigation system with 3 degrees of freedom," *Int. J. Comput. Assist. Radiol. Surg.*, vol. 11, no. 8, pp. 1537–1545, Aug. 2016.

[27] K. Lee *et al.*, "MR safe robotic manipulator for MRI-guided intracardiac catheterization," *IEEE/ASME Trans. Mechatronics*, vol. 23, no. 2, pp. 586–595, Apr. 2018.

[28] M. E. M. K. Abdelaziz *et al.*, "Toward a versatile robotic platform for fluoroscopy and MRI-guided endovascular interventions: A pre-clinical study," in *Proc. IEEE/RSJ Int. Conf. Intell. Robots Syst.*, 2019, pp. 5411–5418.

[29] H. Rafii-Tari *et al.*, "Objective assessment of endovascular navigation skills with force sensing," *Ann. Biomed. Eng.*, vol. 45, no. 5, pp. 1315–1327, May 2017.

[30] C. J. Payne, H. Rafii-Tari, and G.-Z. Yang, "A force feedback system for endovascular catheterisation," in *Proc. IEEE/RSJ Int. Conf. Intell. Robots Syst.*, 2012, pp. 1298–1304.

[31] V. Groenhuis and S. Stramigioli, "Rapid prototyping high-performance MR safe pneumatic stepper motors," *IEEE/ASME Trans. Mechatronics*, vol. 23, no. 4, pp. 1843–1853, Aug. 2018.

[32] V. Groenhuis and S. Stramigioli, "Laser-cutting pneumatics," *IEEE/ASME Trans. Mechatronics*, vol. 21, no. 3, pp. 1604–1611, Jun. 2016.

[33] G. Dagnino *et al.*, , "Haptic feedback and dynamic active constraints for robot-assisted endovascular catheterization," in *Proc. IEEE/RSJ Int. Conf. Intell. Robots Syst.*, 2018, pp. 1770–1775.

[34] S. G. Hart and L. E. Staveland, "Development of NASA-TLX (Task Load Index): Results of empirical and theoretical research," in *Human Mental Workload, Ser. Advances in Psychology*, P. A. Hancock and N. Meshkati, Eds. North-Holland, 1988, vol. 52, pp. 139–183.

[35] J. R. Lewis, "An after-scenario questionnaire for usability studies: Psychometric evaluation over three trials," *SIGCHI Bull.*, vol. 23, no. 4, p. 79, Oct. 1991.

[36] S. Schumann *et al.*, "X-ray image calibration and its application to clinical orthopedics," *Med. Eng. Phys.*, vol. 36, no. 7, pp. 968–974, 2014.

[37] T. MacFarland, *Two-Way Analysis of Variance: Statistical Tests and Graphics Using R, Ser. Springer Briefs in Statistics*. New York, NY, USA: Springer, 2011.

[38] C. Duran, A. B. Lumsden, and J. Bismuth, "A randomized, controlled animal trial demonstrating the feasibility and safety of the magellan endovascular robotic system," *Ann. Vasc. Surg.*, vol. 28, no. 2, pp. 470–478, Feb. 2014.

[39] W. Chi *et al.*, "Collaborative robot-assisted endovascular catheterization with generative adversarial imitation learning," in *Proc. IEEE Int. Conf. Robot. Automat.*, 2020, pp. 2414–2420.